Journal of Solid State Chemistry **158,** 119–133 (2001)
doi:10.1006/jssc.2000.9059, available online at http://www.idealibrary.com IDEAL®

Structures and Textures of Transparent Conducting Pulsed Laser Deposited In_2O_3–ZnO Thin Films Revealed by Transmission Electron Microscopy

L. Dupont,[1] C. Maugy, N. Naghavi, C. Guery, and J.-M. Tarascon

Laboratoire de Réactivité et Chimie des Solides, Université de Picardie Jules Verne, UMR 6007, 33 rue Saint Leu, F-80039 Amiens, France

Received August 14, 2000; in revised form November 14, 2000; accepted December 8, 2000; published online April 5, 2001

Thin films of composition belonging to the In_2O_3–ZnO binary system were made by pulsed laser deposition, and characterized by means of X-ray and transmission electron microscopy (TEM) measurements to obtain phase purity and textural/microstructural information. Collected TEM images together with their analysis clearly show that three different types of films could be obtained, depending on the In_2O_3–ZnO target composition and film growth parameters. The first type, obtained from indium-rich pellets, is made of polyhedral grains having a bixbyite-type structure. The second type, obtained from zinc-rich pellets, presents a classic columnar texture consisting of grains having a wurtzite-type structure, occasionally faulted. The last type of thin films is made of a multitude of $Zn_kIn_2O_{k+3}$ polytypes forming a fibrous texture. The overall EDS analysis evidences that the composition is nearly constant between the target and the film, except for the Zn amount that is always slightly lower in the films. High-resolution electron microscopy studies on films formed of polytypes enable, after a complete image analysis, a simulation of the X-ray diffraction patterns that fit well with the experimental patterns, justifying the validity of our random intergrowth model. © 2001 Academic Press

INTRODUCTION

Transparent conducting oxide (TCO) films are widely used in optoelectronic devices (e.g., electrochromic plasma displays and others). Tin-doped indium oxide (ITO) is the most commonly used TCO material because of its high conductivity and optical transparency properties. However, many studies have been devoted to the search for a new, cheaper TCO offering similar or even better performance (e.g., lower resistivity, higher transparency window) (1–7). Recently, research has been oriented toward zinc indium oxides (8–10). Moriga *et al.* (11) studied the structures and physical properties of phases obtained in the system In_2O_3–ZnO, and revealed, in the bulk stage, nine polytypes having the $Zn_kIn_2O_{k+3}$ composition ($k = 3$, 4, 5, 6, 7, 9, 11, 13, and 15). Besides composition, obtaining a single-phase polymorph strongly depended on the synthesis conditions, namely annealing temperature, atmosphere, and so on. This dependence was even enhanced when these materials were grown as thin films by either pulsed laser deposition or other techniques. Interestingly, the stabilization of other polymorphs such as $Zn_2In_2O_5$ could be achieved depending on the thin-film growth parameter. A general experimental trend, however, between bulk and thin-film materials, is that the latter constantly showed better conductivity. Could such a difference be nested in some peculiar textural/microstructural aspect of the PLD deposited films? In order to check for the existence of a correlation between thin-film structures and physical properties, their microstructure was studied. The structural characterization of films is complicated because of the preferential orientation of all the phases in this system, namely their growth in the *c* direction as determined by X-ray diffraction (10, 12). This certainly explains why there are only a few articles on the structural characterization of In_2O_3–ZnO thin films (9, 12) while numerous studies exist on $Zn_kIn_2O_{k+3}$ bulk characterization (8, 12–17). Thus, the challenge was to find a suitable technique for the characterization of such films.

High-resolution transmission electron microscopy (HRTEM), combined with other microscopy techniques (selected area electron diffraction (SAED), EDS), turned out to be a powerful technique to locally characterize the thin-film texture, composition, and local atomic ordering. For the first time, to our knowledge, this technique will allow us to answer questions about the microstructure of the so-obtained phases as well as whether the structure of the nine $Zn_kIn_2O_{k+3}$ composition polytypes ($k = 3$, 4, 5, 6, 7, 9, 11, 13, and 15) between the pellet and the film is preserved.

[1]To whom correspondence should be addressed. E-mail: loic.dupont@sc.u-picardie.fr.

0022-4596/01 $35.00

This paper is organized as follows. First, a short review of the involved structures, together with the characterization of the studied samples, is given in order to show the X-ray diffraction technique limitations, and to set up the second part of this manuscript, which will be focused mainly on HRTEM results. Finally, in the third part, experimental X-ray diffraction data will be correlated with the simulated X-ray pattern obtained from microscopy image interpretations to test the representativeness of HRTEM analysis.

EXPERIMENTAL TECHNIQUES

Synthesis and Deposition Conditions

Indium–zinc oxide thin films were deposited on a 1 cm^2 glass substrate by pulsed laser deposition (PLD) using a KrF excimer laser beam (Lambda Physik, compex 102, $\lambda = 248$ nm) with a laser fluence of 1–2 J/cm^2. The base pressure in the chamber was of the order of 10^{-6} mbar, and deposition times were 40 mins with a repetition rate of 10 Hz (0.16 to 0.23 Å/shot). The substrate temperature and the oxygen pressure were fixed at 500°C and 10^{-3} mbar, respectively. The targets were either pellets of ZnO and In_2O_3 mixtures in stoichiometric proportions or monophasic $Zn_kIn_2O_{k+3}$ ($3 \leq k \leq 15$). These last pellets were obtained using the ceramic process reported by Moriga *et al.* (11). For the former, stoichiometric proportions were heated for 5 days at 1250°C, and quenched to room temperature in order to produce targets with a density between 80–90% of the theoretical value. All the studied samples with their code names as well as their nominal compositions are reported in Table 1. The variable x refers to the Zn/(Zn + In) ratio.

Transmission Electron Microscopy

Films chips were scratched from the glass substrate using a diamond tip. A small amount of the recovered sample was dispersed by manual grinding in 1-butanol. A drop of the suspension was collected on a holey carbon film supported on a Cu grid. Both bright-field and HRTEM studies were performed with a Jeol 2010 microscope having a point resolution of 2 Å, and equipped with EDS analyzer (Oxford).

TABLE 1

Code name	Nominal composition	x = Zn/(Zn + In) ratio
ARZN30-170	$Zn_{0.3}In_{1.7}O_{2.58}$	0.15
ARZN50-150	$Zn_{0.5}In_{1.5}O_{2.75}$	0.25
ZN1	$Zn_1In_2O_4$	0.33
ZN2	$Zn_2In_2O_5$	0.5
ZN3[a]	$Zn_3In_2O_6$	0.6
ZN5[a]	$Zn_5In_2O_8$	0.71
ZN7[a]	$Zn_7In_2O_{10}$	0.78
ZN11[a]	$Zn_{11}In_2O_{14}$	0.85
ZN15[a]	$Zn_{15}In_2O_{18}$	0.88
ARZN92-8	$Zn_{0.92}In_{0.08}O_{1.04}$	0.92
ARZN95-5	$Zn_{0.95}In_{0.05}O_{1.025}$	0.95
ARZN98-2	$Zn_{0.98}In_{0.02}O_{1.01}$	0.98

[a]Monophasic $Zn_kIn_2O_{k+3}$ pellets.

Powder Diffraction Techniques

X-ray diffraction was performed on a Philips PW1710 diffractometer with Cu $K\alpha$ monochromatic radiation. The X-ray diffraction pattern was checked for each TEM-studied sample. Simulated X-ray diffraction patterns were calculated using the analysis method of Hendricks and Teller (18) and the HRTEM image interpretations.

RESULTS AND DISCUSSION

(1) Structure Description

It is useful to start with an appropriate description of the In_2O_3 bixbyite (19), ZnO wurtzite (20), and $Zn_kIn_2O_{k+3}$ (11, 13) structures in terms of oxygen and metal atom layer stacking.

The complex bixbyite structure is usually described in terms of the fluorine CaF_2 structure and thought of as an incomplete cubic close-packing of oxygen ions: the indium atoms are distributed as the calcium atoms in the fluorine while the oxygen atoms occupy three-fourths of the fluorine positions. A view of the structure (Fig. 1a) along $[11\bar{2}]$ evidences the oxygen and indium (octahedral InO_6) layer stacking along the [111] direction. Based on the cell parameters and space group (19), the interval between two indium layers is equal to the (222)-type lattice fringe spacing ($d = 2.92$ Å).

The well-known wurtzite structure can be described as a hexagonal close-packing of oxygen, in which only half of the tetrahedral sites are filled with zinc atoms. In this case, the structure consists of layers of ZnO_4 (or equivalently OZn_4) tetrahedra, stacking along the c axis (Fig. 1b), connected via the apices and arranged in an *ABAB* stacking sequence. It is worth noting on the wurtzite unit cell (20) that the interval between two zinc layers is equal to the (002) 2.603 Å fringes.

Finally, using the two previous structure types, the $Zn_kIn_2O_{k+3}$ structures which crystallize in hexagonal unit cells can be roughly visualized (Fig. 1c) as a periodic intergrowth of pure InO_6 octahedra (InO_2^-) layers from bixbyite structure in an $((In_{1/k+1}Zn_{k/k+1})O^{1/(k+1)+})$ wurtzite-type structure matrix, or more simply as the appearance of periodic cubic stacking faults (c) in a hexagonal stacking matrix (h). The so-obtained basic structural unit, projected on the b axis, is presented (Fig. 1c) using $Zn_5In_2O_8$ as an example. More specifically, on the basis of the large amount of structural work performed by Moriga *et al.* (11) on these phases,

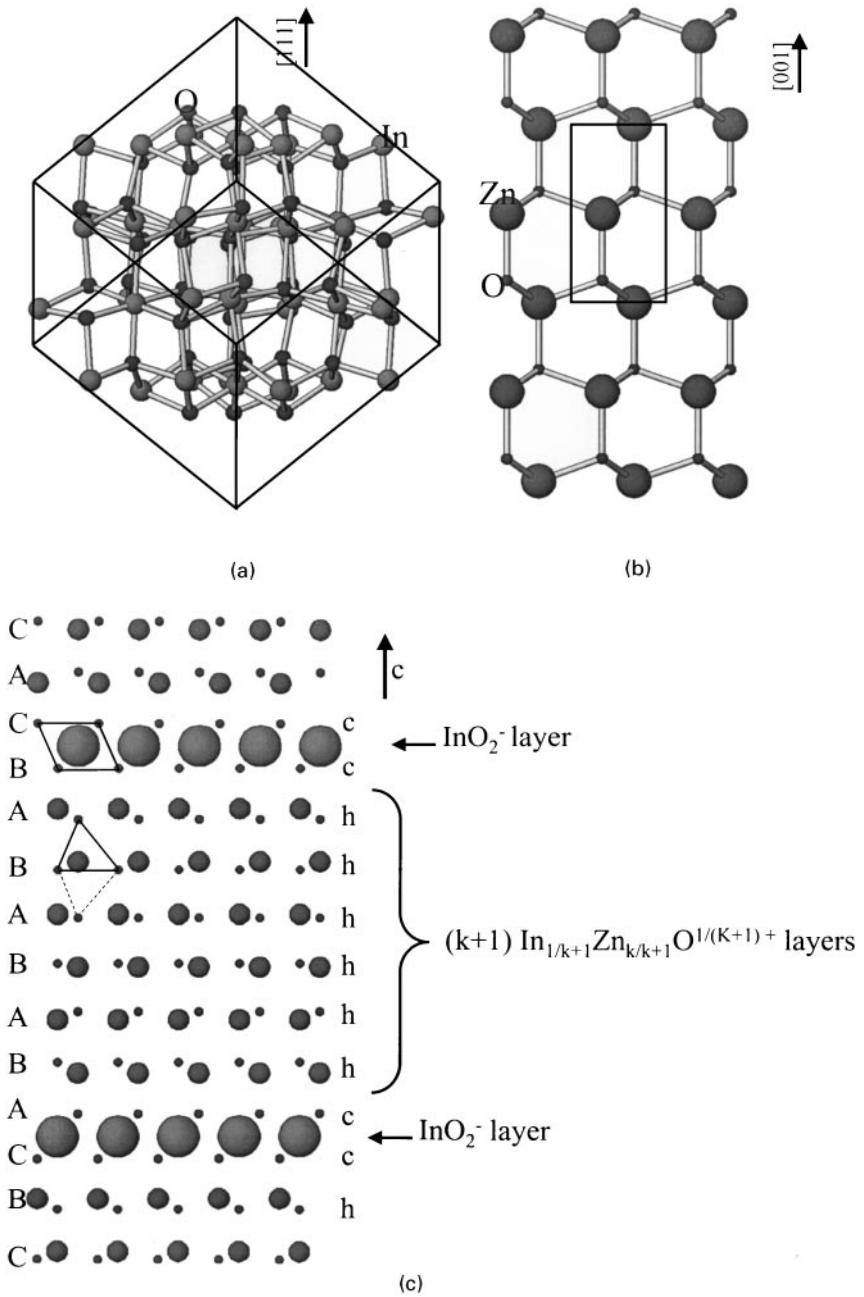

FIG. 1. Projected structure of (a) In_2O_3 bixbyite-type structure along [11$\bar{2}$], (b) ZnO wurtzite-type structure along [100], and (c) layered $Zn_kIn_2O_{k+3}$ polytype structure (namely $Zn_5In_2O_8$) along [010]. Indium, zinc, and oxygen atoms are shown as large, medium, and small spheres, respectively.

the $Zn_kIn_2O_{k+3}$ polytypes can be considered as layered structures with $R\bar{3}m$ space group when k is an odd number and $P6_3/mmc$ when k is an even number. Nevertheless, the occupation of the tetrahedral or trigonal bipyramidal sites in the In/Zn layer remains very controversial. The projected structure presented in Fig. 1c shows that a slight displacement of the In/Zn layer will induce a geometrical change of the cation oxygen coordination (from tetrahedral to trigonal bipyramidal). The aim of our paper is not to discuss the fine structure of each polytype but rather to focus on the characteristic stacking sequences of each polytype in order to establish a TEM database that could be routinely used, at a later stage, to rapidly determine the thin-film polytype composition. First, using only h and c stackings, the variation of the space group versus the parity of the k number in $Zn_kIn_2O_{k+3}$ could be explained. Indeed, if k is odd, the structure will be described by an even number of $(In_{1/k+1}Zn_{k/k+1})O^{1/(k+1)+}$ hexagonal packed layers

interleaved by InO_2^- cubic packed layers. The close-packing sequence will be in this case

$$cc \underbrace{h}_{k+1 \text{ times}} cc$$

and the oxygen layers stacking

$$\left(\left| \underbrace{AB}_{k-1 \text{ times}} \right| \underbrace{CA}_{k-1 \text{ times}} \left| \underbrace{BC}_{k-1 \text{ times}} \right| \right),$$

revealing that three basic structural units $\{InO_2^-/(K+1)(In_{1/k+1}Zn_{k/k+1})O^{1/(k+1)+}/InO_2^-\}$ should be used to find the true periodicity indicating a trigonal symmetry. In contrast, if k is even, the close-packing sequence will be

$$cc \underbrace{h}_{k+1 \text{ times}} cc$$

while the oxygen layers stacking will be quite different

$$\left(\left| \underbrace{AB}_{k-1 \text{ times}} A \right| C \underbrace{BC}_{k-1 \text{ times}} \right)$$

and only two basic structural units should be used to find the true periodicity indicating the hexagonal symmetry.

Such an effect of the c and h stacking sequences on the symmetry (hexagonal or trigonal) is well known for hexagonal perovskites (21–23). For the latter, it was shown that the TEM image contrast changes were very sensitive to close-packing changes, enabling us to clearly identify the hexagonal polytypes (21–23). Since the $Zn_kIn_2O_{k+3}$ structures are extremely sensitive to close-packing changes driven by changes in the chemical nature of the cations layers, the HRTEM technique was similarly used (12–17, 24).

In summary, the periodicity of the cubic close-packed InO_2^- layers (or the number of Zn/In layers interleaved) as determined by TEM can be used to identify a given $Zn_kIn_2O_{k+3}$ structure. This periodicity could be translated in terms of spacing between two consecutive pure indium layers. Starting from the In–In structural distance, and using the spacing reported for known polytypes (11), a table linking the supposed chemical composition, the number of interleaved In/Zn layers, and the height of the basic structural unit is proposed for all the imaginable polytypes (Table 2). This tool will be useful for the interpretation of TEM images (discussed later).

TABLE 2

Chemical formula	Number of $((In_{1/k+1}Zn_{k/k+1})O^{1/(k+1)+})$ layers interleaved by pure InO_2^- sheets between pure indium sheets	u_j values spacing (Å)	Layer/layer average distance (Å)
In_2O_3	0	2.92[a]	2.92
	1	5.80[b]	2.90
$Zn_1In_2O_4$	2	8.63[b]	2.88
$Zn_2In_2O_5$	3	11.42[b]	2.86
$Zn_3In_2O_6$	4	14.17[c]	2.83
$Zn_4In_2O_7$	5	16.76[c]	2.79
$Zn_5In_2O_8$	6	19.37[c]	2.77
$Zn_6In_2O_9$	7	21.98[c]	2.75
$Zn_7In_2O_{10}$	8	24.56[c]	2.73
$Zn_8In_2O_{11}$	9	27.17[b]	2.72
$Zn_9In_2O_{12}$	10	29.75[c]	2.70
$Zn_{10}In_2O_{13}$	11	32.37[b]	2.70
$Zn_{11}In_2O_{14}$	12	34.98[c]	2.69
$Zn_{12}In_2O_{15}$	13	37.56[b]	2.68
$Zn_{13}In_2O_{16}$	14	40.12[c]	2.67
$Zn_{14}In_2O_{17}$	15	42.73[b]	2.67
$Zn_{15}In_2O_{18}$	16	45.33[c]	2.67
$Zn_{16}In_2O_{19}$	17	47.92[b]	2.66
$Zn_{17}In_2O_{20}$	18	50.51[b]	2.66
$Zn_{18}In_2O_{21}$	19	53.09[b]	2.65
$Zn_{19}In_2O_{22}$	20	55.66[b]	2.65
$Zn_{20}In_2O_{23}$	21	58.22[b]	2.65
$Zn_{21}In_2O_{24}$	22	60.78[b]	2.64
$Zn_{22}In_2O_{25}$	23	63.32[b]	2.64
$Zn_{23}In_2O_{26}$	24	65.86[b]	2.63
$Zn_{24}In_2O_{27}$	25	68.39[b]	2.63
$Zn_{25}In_2O_{28}$	26	70.91[b]	2.62
$Zn_{26}In_2O_{29}$	27	73.43[b]	2.62
$Zn_{27}In_2O_{30}$	28	75.94[b]	2.62
$Zn_{28}In_2O_{31}$	29	78.43[b]	2.61
$Zn_{29}In_2O_{32}$	30	80.92[b]	2.61

[a]Spacing calculated from the In_2O_3 structure (13).
[b]Values extrapolated from known ones.
[c]Values proposed by Moriga *et al.* (16).

(2) X-Ray Diffraction Study

As reported previously (9), whatever the pellet composition, XRD patterns obtained on films exhibit only one strong reflection. At low zinc content ($x \leq 0.25$) or at high zinc content ($x \geq 0.9$), this peak was ascribed to the cubic In_2O_3-type structure (Fig. 2a) or to the ZnO-type structure (Fig. 2b), respectively. In the composition range between the two previous domains ($0.25 < x < 0.9$), only one intense Bragg peak surrounded by weak reflections is observed (Fig. 2c). In this composition domain, the observed peak that is shifting toward a high 2θ angle when k increases was attributed to a $00l$ reflection of the layered $Zn_kIn_2O_{k+3}$-type structure, implying a very strong orientation of the thin films along the c axis (9, 11). Although general considerations could be extracted from these patterns, numerous questions remain unanswered. Among them are, for instance:

(1) The origin of the peak broadening (Fig. 2a) as well as that of the increased preferential orientation of the indium-rich films as the zinc content is increased.

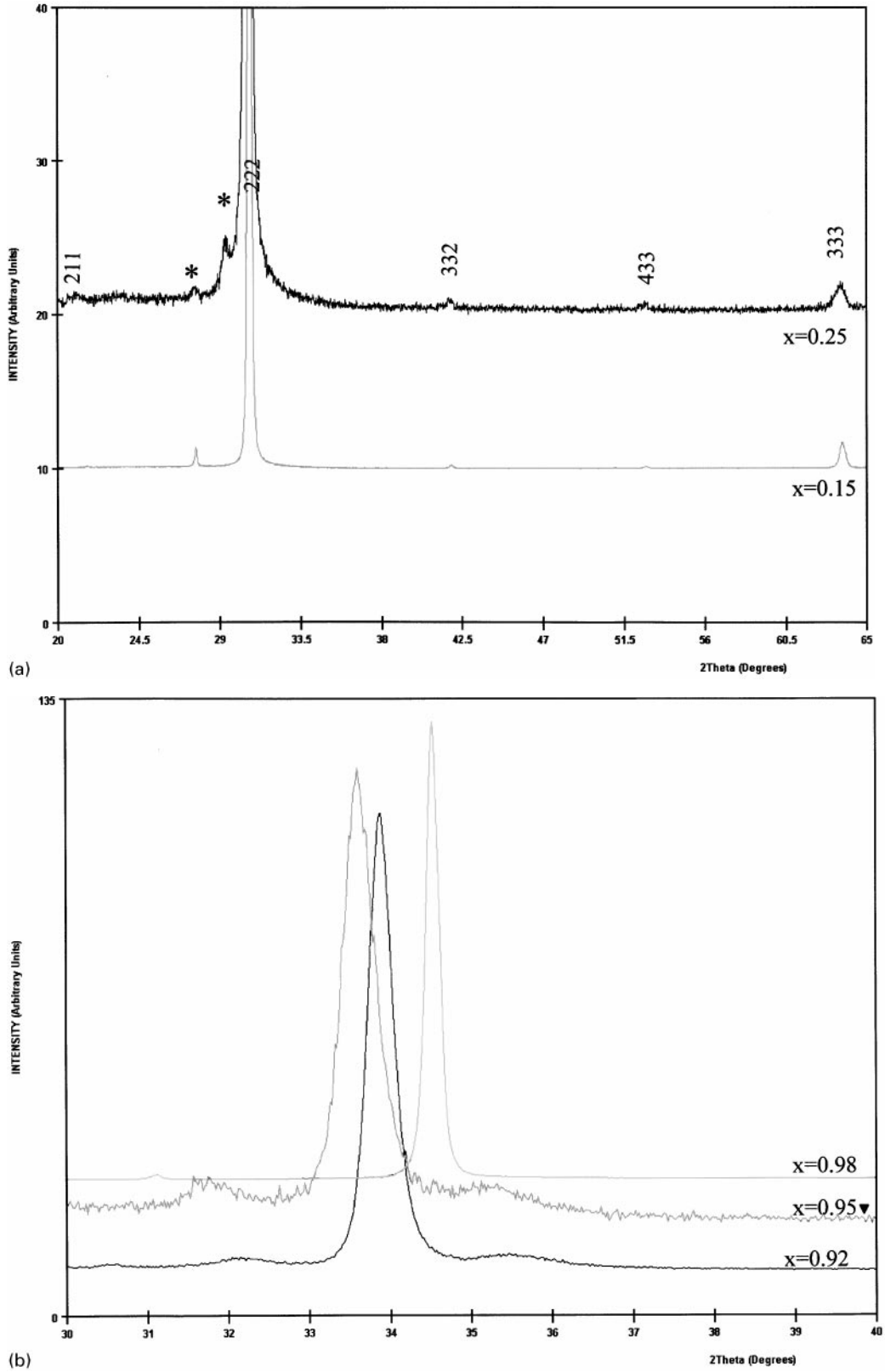

FIG. 2. X-ray diffraction patterns obtained on films deposited using (a) indium-rich targets, (b) zinc-rich targets (▼ refers to a nominal composition, the measured composition is $x = 0.9$), and (c) targets with a composition range $0.33 \leq x \leq 0.88$ (arrows indicate the reflection feet). Asterisks refer to reflections due to parasite copper radiations. x refers to the Zn/(Zn + In) atomic ratio.

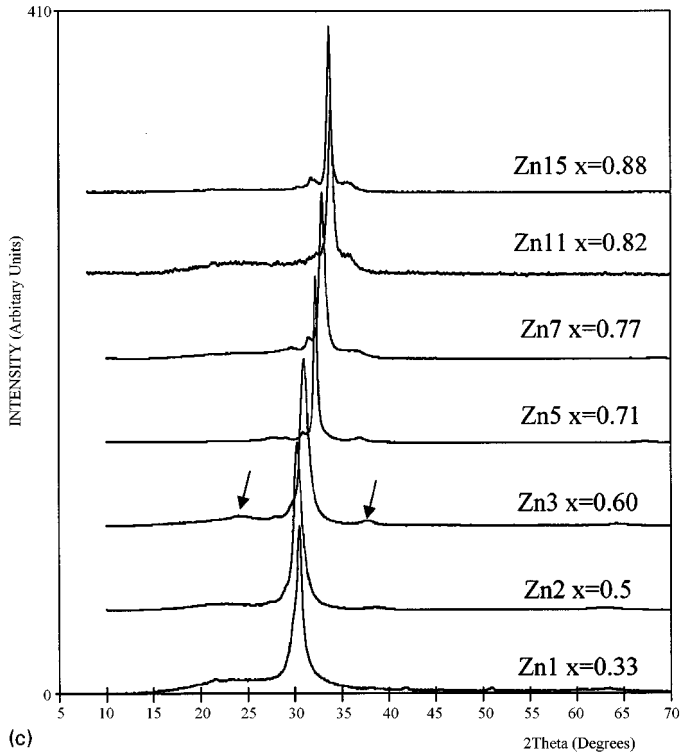

FIG. 2—*Continued*

(2) The true meaning of the reflection shift toward a high 2θ angle observed for $Zn_kIn_2O_{k+3}$ polytypes with increasing k.

(3) The origin of the peak feet observed on most of the thin-film XRD patterns.

Thus, to tentatively answer these issues, the local structure, texture, and morphology of the laser-ablated films were studied by TEM.

(3) TEM Study

(a) Film textures and composition evolution. Depending on the part of the In_2O_3–ZnO binary phase diagram considered, three different film textures were observed during this study.

The films obtained from a pellet having a composition lower than $x = 0.35$ were granular and formed by grains having a cubic shape (Fig. 3a). In addition, as the amount of zinc was increased, the grain size decreased from about 500 Å (Fig. 3a) for the $x = 0.15$ sample to about 250 Å for the $x = 0.25$ sample (Fig. 3b). This suggests that the peak broadening observed in the X-ray patterns is nested in Zn-driven grain size differences. From the measured crystallite sizes of the two previous samples and the Scherrer formula (25), we deduced that the peak's full width at half-maximum (FWHM) should be multiplied by 2 between the $x = 0.15$ to $x = 0.25$ samples. This is in good agreement with the 0.158° and 0.318° (2θ) FWHM measured for the peaks corresponding to the $x = 0.15$ and $x = 0.25$ samples, respectively. However, this finding does not allow for polycrystalline grains and local structural faults within these film compositions.

The films obtained from pellets having a composition range between $x = 0.35$ and $x = 0.9$ have a fiber-type texture as shown by the bright-field images taken for the $x = 0.6$ and $x = 0.5$ samples (Figs. 3c, 3d, 3e), respectively. This texture is consistent with the strong orientation observed on the X-ray patterns. In this case, the film could no longer be assimilated to a granular but rather to a large crystallite dimension, leading to the expectation of an X-ray diffraction pattern having sharp peaks. The measured FWHM values ranging from 0.420° ($x = 0.71$) to 1.230° ($x = 0.33$) are larger than those previously measured on granular films, suggesting that they contain numerous crystallites and faults not visible on low-magnification bright-field images, as will be confirmed later. It is worth noting that the texture of the Zn15 sample (Fig. 3e) film is midway between those of $Zn_kIn_2O_{k+3}$ films and the zinc-rich films presented below.

The zinc-rich sample films have a columnar-type texture (Figs. 3f, 3g, 3h) similar to that of the pure zinc oxide (26). The bright-field image obtained from the $x = 0.92$ sample (Fig. 3f) bears some resemblance to the one obtained from the sample with $x = 0.98$ (Fig. 3h), with rectangular columnar grains parallel to each other. In contrast, the image for the $x = 0.95$ sample (Fig. 3g) bears a close resemblance to the one collected from the ZN15 sample (Fig. 3e) in which the rectangular grains are not parallel. Let us return to the X-ray data obtained on similar films (Fig. 2c). Although the main trend is the observation of a narrow peak (FWHM range from 0.15 to 0.3° in 2θ) shifting toward high angles with increasing zinc content, one can note that for the sample with $x = 0.95$ the peak is quite large (0.5° 2θ) and located at a lower 2θ value. Using the same target, this result was reproducible, ruling out experimental artifacts. The origin of such a difference was found by checking by EDS the composition of the target, which differed from the nominal composition with namely a lower amount of zinc.

This deviation was not specific to the $x = 0.95$ sample. The overall evolution of the film composition is plotted in Fig. 4 together with the target composition for the various samples. Through the series, the larger composition difference between the film and the target is obtained for samples having $x < 0.7$, with the thin-film composition always smaller than the target one. The hypothesis of zinc volatility during the annealing or laser deposition process could be put forward to explain this difference. Note that the maximum in composition variation during the deposition process is obtained for samples suspected to have a layered $Zn_kIn_2O_{k+3}$ structure, suggesting that besides the technological parameters the obtained host structure may have an influence upon the zinc loss.

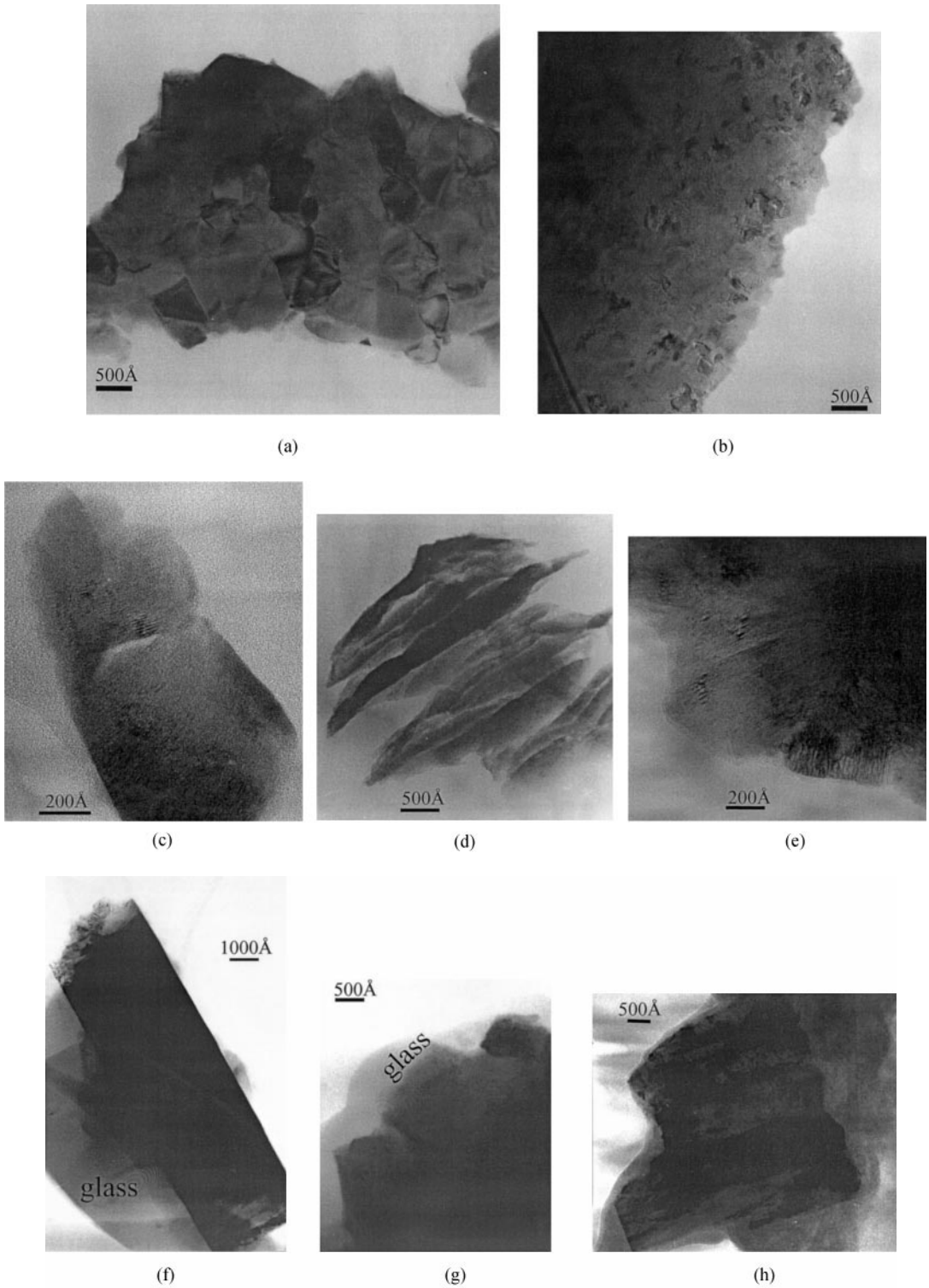

FIG. 3. Bright-field images obtained on (a) ARZN30-170 ($x = 0.15$), (b) ARZN50-150 ($x = 0.25$), (c) ZN2 ($x = 0.5$), (d) Zn3 ($x = 0.6$), (e) Zn7 ($x = 0.78$), (f) ARZN92-8 ($x = 0.92$), (g) ARZN95-5 ($x = 0.95$), and (h) ARZN98-2 ($x = 0.98$) samples. x refers to the Zn/(Zn + In) atomic ratio.

(b) High-resolution transmission electron microscopy study. We will now study the three structural ranges (In_2O_3 structure for the indium-rich part, ZnO structure for the zinc-rich part, and $Zn_kIn_2O_{k+3}$ structure for the remaining midway domain), suspected to exist within the In_2O_3–ZnO phase diagram.

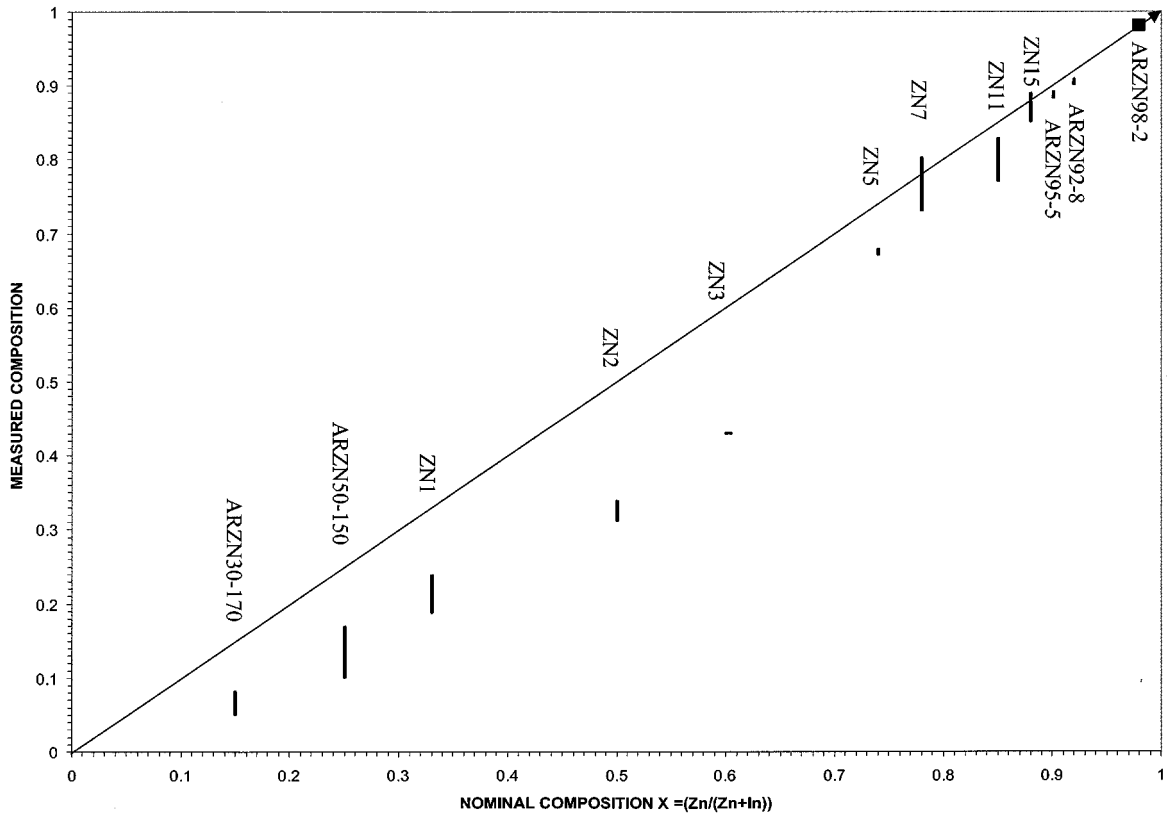

FIG. 4. Graph showing the composition of the films measured by EDS versus the nominal composition of the target.

(3-b-α) Indium-rich part: the In_2O_3-type structure. Both high-resolution images and SAED patterns confirm the In_2O_3-type structure assignment for this part of the binary diagram. The images (Fig. 5a) obtained on the $x = 0.15$ sample show large and well-crystallized domains having lattice fringes of 2.9 Å, consistent with the In_2O_3 (222) spacing. Moreover, the corresponding SAED pattern gives a pattern similar to the one obtained on In_2O_3 along the $[0\bar{1}1]$ zone axis. The weak arches and dots are the contribution from the neighboring crystallites. As the zinc content increases, the crystallite size decreases; for the $x = 0.25$ sample for instance, the crystallite size is smaller than the selected area aperture so that punctual SAED can no longer be achieved and rings are observed (Fig. 5b). All the rings could be indexed using the In_2O_3 cell parameters. It is worth noting that the rings are thin, reflecting small domains having high crystallinity. Therefore, the small and well-crystallized crystallites observed on the HREM image support the above remarks.

In summary, for the indium-rich composition domain the films are composed of grains having a bixbyite-type structure, which is preserved up to a zinc atomic amount of $\frac{1}{3}$. The insertion of such a level of zinc in the host structure does not induce a drastic change in the cell parameters nor in the crystallinity of the grain building the film, but does affect the grain size. Strain induced by zinc atoms inside the In_2O_3 structure could be proposed to explain this phenomenon. The higher the zinc amount is, the stronger the strain will be, and the smaller the grains will be.

(3-b-β) Presence domain of $Zn_kIn_2O_{k+3}$-type structure. All the images presented herein will show that grains are never made of only one $Zn_kIn_2O_{k+3}$-type structure but of layered intergrowth structures with numerous stacking faults. Thus, this part is devoted to the counting of different polytypes within a sample. In this study numerous images, obtained from several grains for each sample, were processed as follows. The polytype nature is first determined by measuring the distance between two pure indium layers (whiter or darker lines on the image contrast) and then by comparing the obtained values with those given in Table 2. The proportion of each polytype is given by the ratio between the sum of the domain lengths of a given polytype and that of all the polytypes as demonstrated for the ZN7 sample (Fig. 6).

On the selected part (Fig. 6), at least five different polytypes are observed. The measured In–In distances of 17, 14, 11, 6, and 3 Å correspond to $Zn_4In_2O_7$, $Zn_3In_2O_6$,

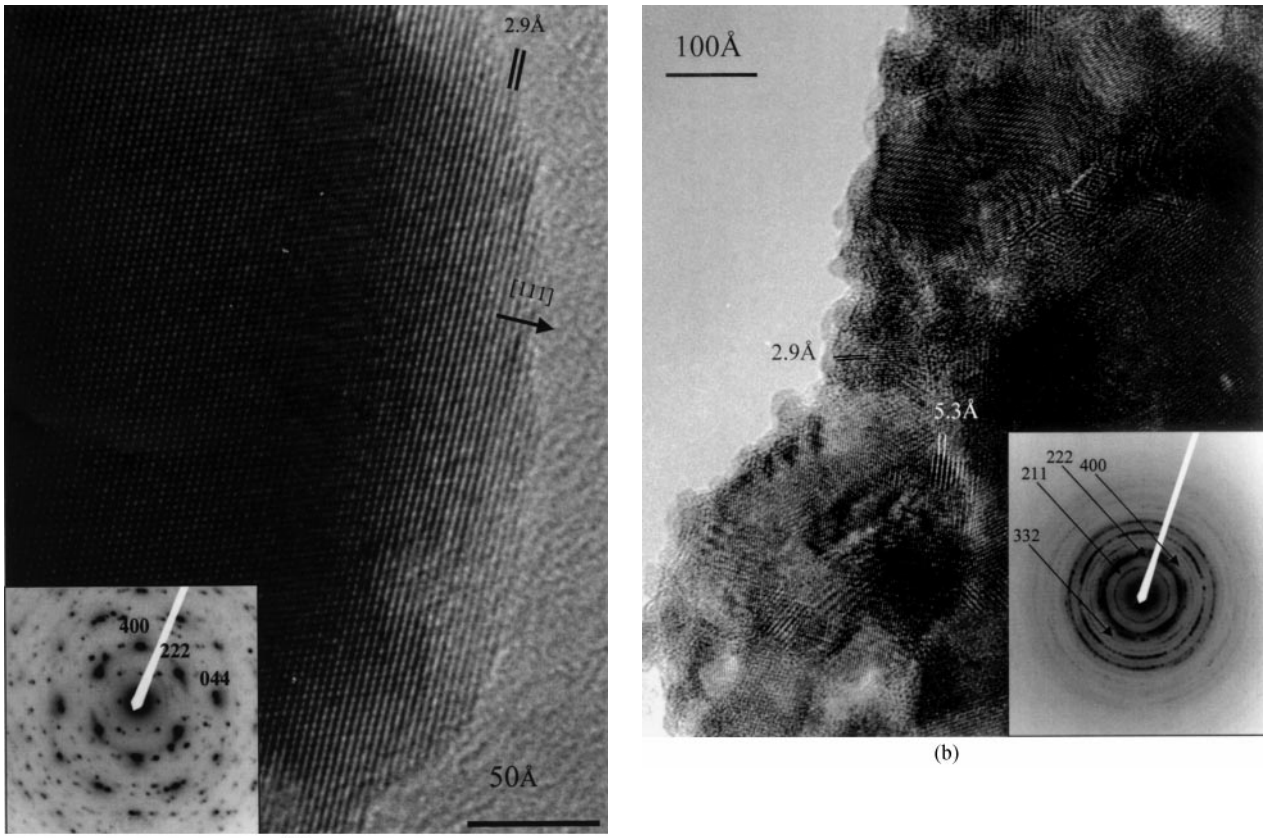

FIG. 5. High-resolution image obtained on indium-rich sample grains: (a) ARZN30-170 ($x = 0.15$) monolithic grain and (b) ARZN50-150 ($x = 0.25$) mosaic film. The corresponding SAED patterns are included in the images and are indexed using the In_2O_3 cell parameters.

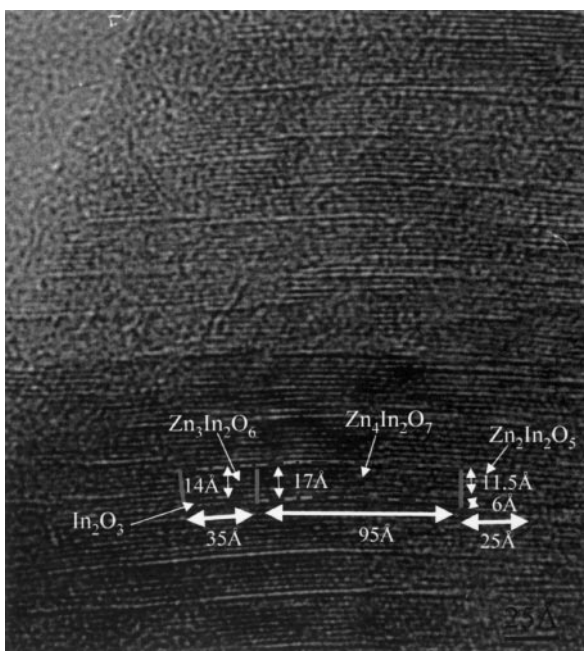

FIG. 6. Image analysis of a Zn7 ($x = 0.78$) HRTEM micrograph. Polytypes' identification as well as the proportion of each phase building-up the film were determined using this method.

and $Zn_2In_2O_5$ polytypes, a polytype having one $((In_{1/k+1}Zn_{k/k+1})O^{1/(k+1)+})$ layer interleaved by two pure InO_2^- sheets, and an In_2O_3-type structure, respectively. Joined end to end, the polytypes' total length is mainly equal to $95 + 35 + 25 + 25 + 35 = 215$ Å. By normalizing to the overall length, the proportion of each phase is obtained and equals 44.2, 16.3, 11.6, 11.6, and 16.3%, respectively. This type of counting should then be extrapolated to the overall image and to other images recorded on this ZN7 sample for good statistics, so as to obtain reliable data for the XRD simulation part. For each graph, the x axis corresponds to the number of $((In_{1/k+1}Zn_{k/k+1})O^{1/(k+1)+})$ layers interleaved by two pure InO_2^- sheets and not to the polytype member k. From that description and using Table 2, one can clearly see that there is a hypothetical midway phase (reported above) between In_2O_3 ($x = 0$) and $Zn_1In_2O_4$. Using such a descriptive approach, we now present the TEM data obtained from various film samples.

(3-b-β-1) ZN1 sample. The so-obtained film is equally made of large grains having the In_2O_3-type structure and small grains having the $Zn_kIn_2O_{k+3}$-type structure as shown in Fig. 7a. A characteristic In_2O_3 SAED pattern could be achieved (Fig. 7b) along the $[0\bar{1}1]$ zone axis. In this

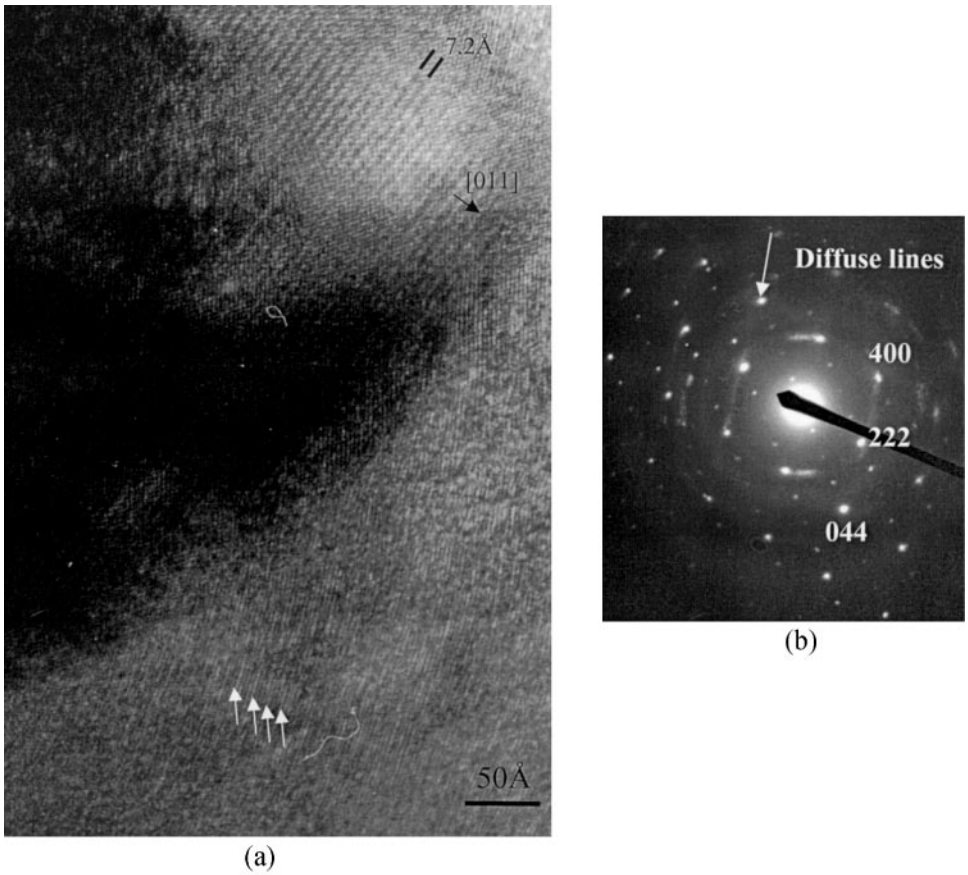

FIG. 7. Micrographs obtained on Zn1 ($x = 0.33$) film. (a) Bright-field image, showing In_2O_3-type structure grain as well as fiber texture grain formed by $Zn_kIn_2O_{k+3}$ polytypes. The white arrows show the indium layers. (b) Corresponding SAED pattern obtained by superposition of In_2O_3 and $Zn_kIn_2O_{k+3}$ SAED patterns. The white arrow shows one of the diffuse lines.

pattern, additional diffuse lines, signifying random stackings of $Zn_kIn_2O_{k+3}$ polytypes, are observed. The proportions of In_2O_3-type phase and each polytype are given in Fig. 8. Interestingly, although it was not perfectly pure, the possibility of stabilizing a $Zn_1In_2O_4$ phase was indicated for the first time by the HRTEM technique.

(3-b-β-2) ZN2 sample to ZN7 sample. As reported in Fig. 8, films obtained from ZN2, ZN3, ZN5, and ZN7 samples are essentially composed for the most part of the polytype corresponding to the k reference of the precursor sample (i.e., $Zn_2In_2O_5$ for the ZN2 sample). The polytype distribution differs from one sample to another with, nevertheless, the percentage of polytypes having ± 1 Zn/In layer compared to the dominant sample being quite large. However, the reported percentage of In_2O_3-type structure, while no In_2O_3-type structure grain was observed, arises from In_2O_3 domains scattered in the polytype matrix of the crystals. From the HRTEM survey of the samples, one can deduce that the average domains size is small, ranging between 5 and 35 Å (Fig. 9).

As shown in Fig. 8, PLD films of only one polytype are difficult to achieve and furthermore we note that the structural homogeneity (in opposition to the composition homogeneity) of the target is not an essential parameter in order to obtain a monophasic film. Indeed, the PLD technique, using pellets made of either monophasic polytypes or a mixture of ZnO and In_2O_3, lead to polyphasic films. This is not surprising since the polytypes only differ from one another by the number of intermediary layers describing the periodicity; one would expect the energy difference between two consecutive polytypes to be low so that random intergrowth of polytypes is quite common and experimentally difficult to bypass. Nevertheless, using the PLD technique, we could stabilize $Zn_kIn_2O_{k+3}$ polytypes ($Zn_1In_2O_4$, $Zn_8In_2O_{11}$, $Zn_{10}In_2O_{13}$, $Zn_{12}In_2O_{15}$) that were not isolated in the bulk stage.

(3-b-β-3) ZN11 and ZN15 samples. As the zinc content increases, we observe the loss in the fiber-type texture as deduced from HREM where the indium layers are no longer parallel to one another (Fig. 10).

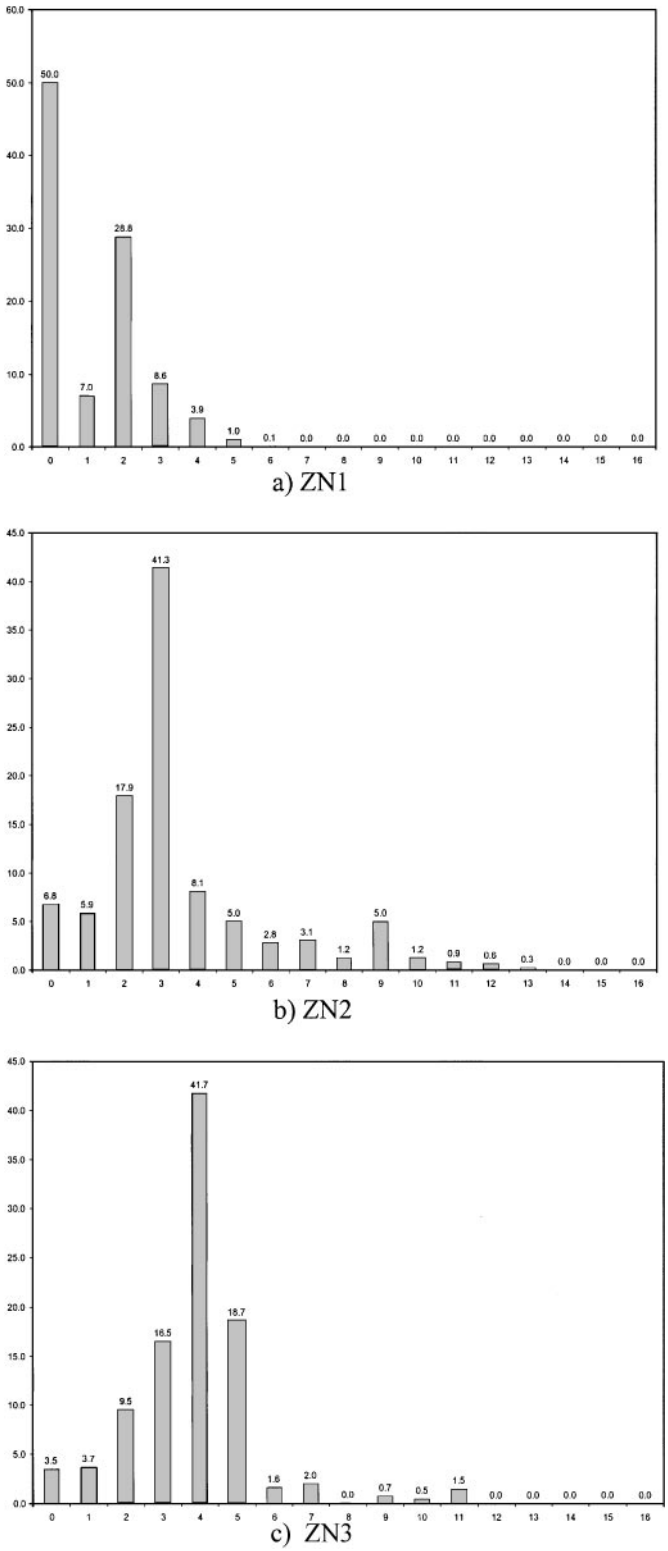

FIG. 8. Statistic graphs obtained from HRTEM image analysis. For each film sample, the percentage of each polytype contained therein is reported. The X axis corresponds to the number of mixed zinc indium layers between two indium layers and, consequently, using Table 2, identifying the polytypes.

The films (ZN11, ZN15) obtained from target made with a high zinc level ($Zn_{11}In_2O_{14}$ and $Zn_{15}In_2O_{18}$) consist of a very large distribution of polytypes (Fig. 8). For instance, for the ZN11 sample film, the dominant polytypes are the $Zn_8In_2O_{11}$ (14.1%) and $Zn_9In_2O_{12}$ (10.4%) polytypes, although they do not have the same composition as the target. Even so, it is worth noting that a significant amount of the expected polytype, $Zn_{11}In_2O_{14}$, is also measured (9.3%).

In comparison with the ZN2 to ZN7 samples, the ZN11 and ZN15 average polytype length is increased to 75 Å (Figs. 9 and 10). This effect could simply arise from the fact that these $Zn_kIn_2O_{k+3}$-rich oxides are built with large ZnO-type structure blocks interleaved with a few InO layers that control the polytype crystallite size. The high zinc content films, made of layers of almost pure zinc interleaved with pure indium layers, have fewer defects (the defect being one indium atom in the zinc layer), and consequently contain larger polytypes domains (Figs. 9 and 10).

(3-b-γ) Zinc-rich part: the ZnO-type structure. The contrast observed in the thin part of one of the ARZN98-2 crystals ($x = 0.98$) fits well with a classic wurtzite-type structure (Fig. 11). The measured fringe distances (2.6 Å) correspond to the (002) spacing. Therefore, the close-packing direction, c axis, could easily be identified on the micrograph. As soon as the thickness increases, the image contrast shows stacking faults along the c axis as well as a few variations in the 002 reticular distances. These faults are probably due to the low amount of indium perturbing the zinc array. The lower the indium content, the fewer faults. As observed in Fig. 2b, the decrease in the amount of materials faults induces a FWHM decrease in the X-ray diffraction patterns.

(4) Simulation of the X-Ray Diffraction According to the Data Recorded by HRTEM

In order to check the representativeness of the statistic data obtained from the HRTEM study, simulations of the obtained thin-film X-ray diffraction patterns were carried out. The patterns could be simulated according to the Hendricks and Teller (18) approach, frequently used in the case of compounds having random polytype intergrowths as follows. Applied to the $Zn_kIn_2O_{k+3}$ system, the X-ray intensity formula proposed by Hendricks and Teller becomes

$$I = |F|^2 \frac{1 - \langle e^{iku} \rangle \langle e^{-iku} \rangle}{1 - \langle e^{iku} \rangle - \langle e^{-iku} \rangle + \langle e^{iku} \rangle \langle e^{-iku} \rangle}$$

where k is the scattering vector, $k = (4\pi/\lambda) \sin\theta$, θ is the Bragg angle, and F is the structure factor for the ZnO or In_2O_3 structure. Since the simulated pattern will be scaled, the absolute value of F is meaningless. Only its variation as a function of the Bragg angle is significant. The value e^{iku} is

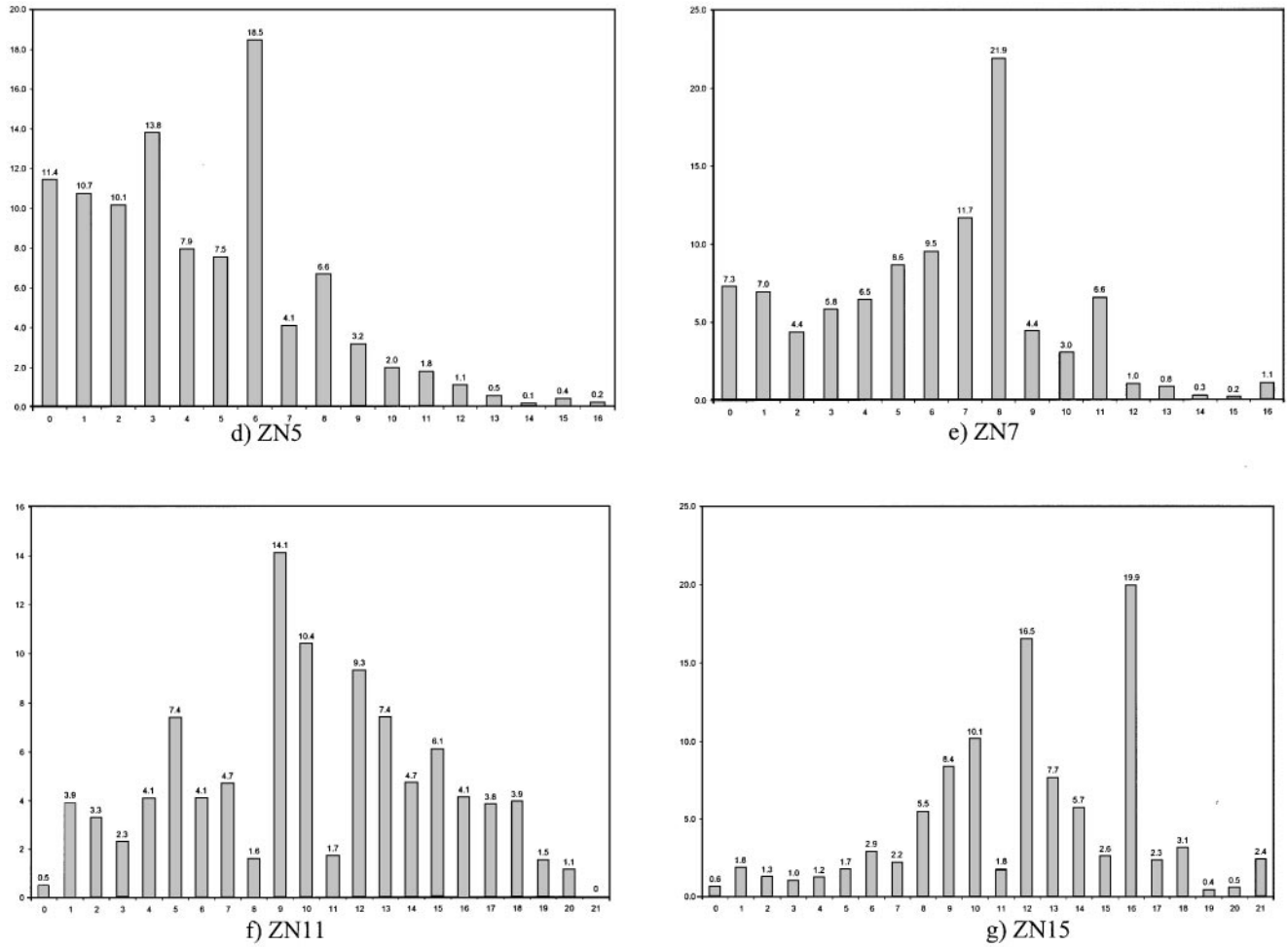

FIG. 8—*Continued*

defined as $\langle e^{iku} \rangle = \sum_{j=0}^{n} p_j e^{iku_j}$ where p_j is the probability of two InO_2^- layers separated by j In/ZnO layers, and u_j is equal to the distance between two consecutive InO_2^- layers along the close-packing direction (Table 2). These values can be read from Fig. 8: for a given graph, p_j corresponds to the y axis value of a column while j corresponds to the x axis value of the same column. For example, the ZN2 X-ray simulation, presented in Fig. 12, is obtained using the following values:

$$\begin{array}{llll} p_0 = 0.068, & u_0 = 2.92\ \text{Å}; & p_1 = 0.059, & u_1 = 5.8\ \text{Å}; \\ p_2 = 0.179, & u_2 = 8.63\ \text{Å}; & p_3 = 0.413, & u_3 = 11.42\ \text{Å}; \\ p_4 = 0.081, & u_4 = 14.17\ \text{Å}; & p_5 = 0.050, & u_5 = 16.76\ \text{Å}; \\ p_6 = 0.028, & u_6 = 19.37\ \text{Å}; & p_7 = 0.031, & u_7 = 21.98\ \text{Å}; \\ p_8 = 0.012, & u_8 = 24.56\ \text{Å}; & p_9 = 0.050, & u_9 = 27.17\ \text{Å}; \\ p_{10} = 0.012, & u_{10} = 29.75\ \text{Å}; & p_{11} = 0.009, & u_{11} = 32.37\ \text{Å}; \\ p_{12} = 0.006, & u_{12} = 34.98\ \text{Å}; & p_{13} = 0.003, & u_0 = 37.56\ \text{Å}. \end{array}$$

In the case of deviation between the experimental and simulated patterns, namely in terms of peak position and width, the representativeness of the HRTEM studies crystals should not immediately be assumed, since the position shift could simply arise from the lack of internal standard, enabling us to make a displacement correction for the experimental pattern. Such a correction is often essential in the case of thin films because of diffractometer geometrical problems (height of the sample).

Figure 12 compares the observed and calculated peaks using our model and the R_p values calculated by the relation $R_p = \sum_i |y_i^{obs} - y_i^{calc}| / \sum_i y_i^{obs}$ over the range of 2θ values delimited by the dashed vertical lines. For the ZN2 sample, the recorded and simulated patterns (Fig. 12) superimpose almost perfectly ($R_p = 4.4\%$), except for the satellite peaks for which the simulation predicts the position but not the intensity. The films having a strong preferential orientation, it is not surprising that the feet reflections are underestimated on the X-ray diffraction pattern, and consequently that the measured and calculated feet intensities do not match. For the ZN7 simulation, the poor calculated R_p value (20.1%) could be explained by the asymmetric shape

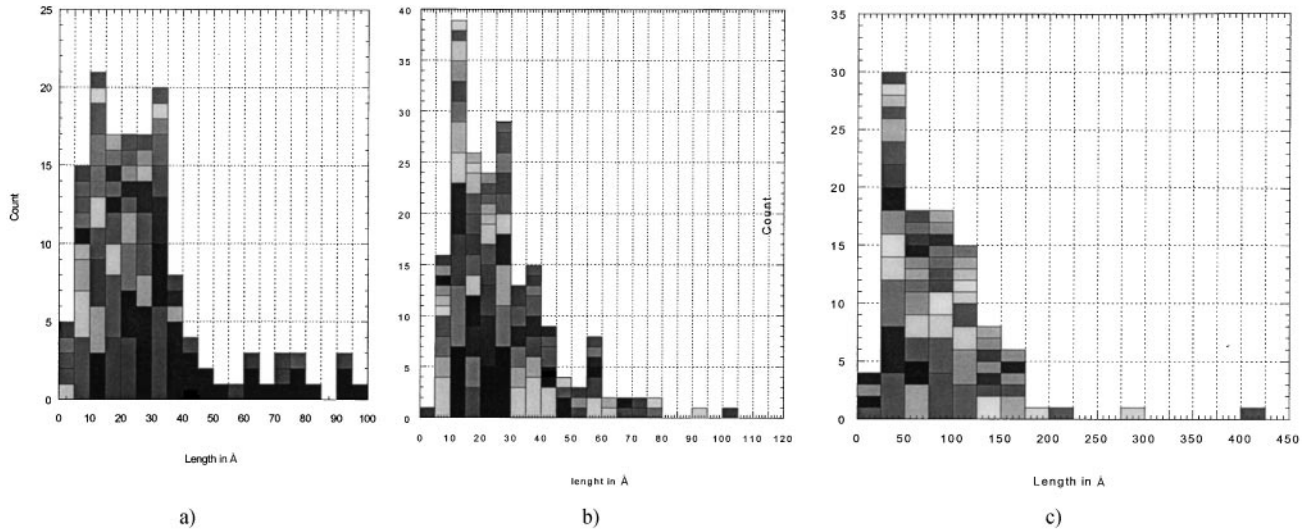

FIG. 9. Graph showing the distribution of polytypes' domains lengths and allowing the determination of the average length of polytypes forming (a) ZN2, (b) ZN5, and (c) ZN11 representative films.

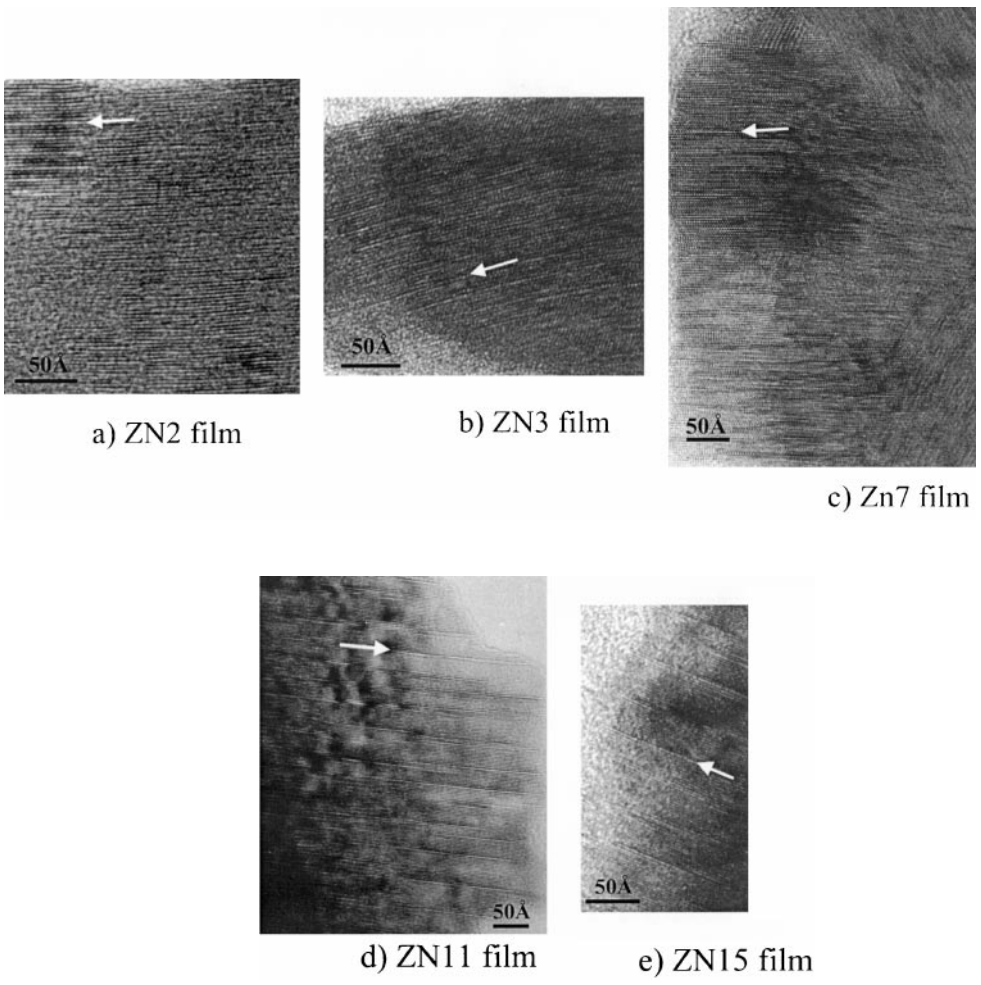

FIG. 10. Representative high-resolution images obtained on (a) ZN2 ($x = 0.5$), (b) ZN3 ($x = 0.6$), (c) ZN7 ($x = 0.78$), (d) ZN11 ($x = 0.85$) and (e) ZN15 ($x = 0.88$) film samples allowing a direct visualization of the polytype mixture and disorder occurring inside the grains. Analyses of these images are a part of the statistics presented in Fig. 8. The white arrows show the contrast associated with pure indium layers.

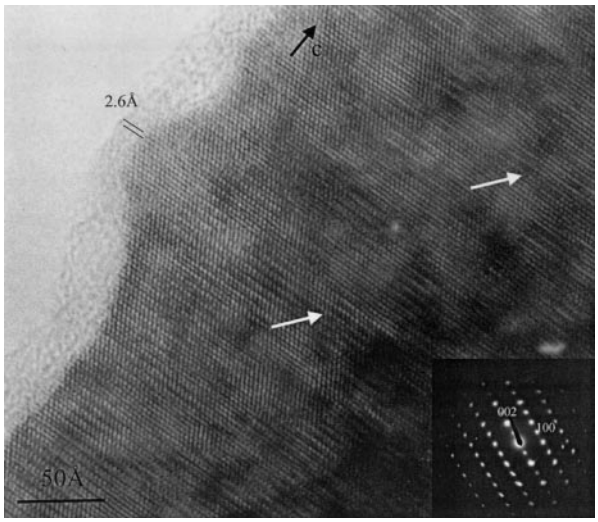

FIG. 11. HREM image realized on the zinc-rich sample ($x = 0.98$). The white arrows indicate variations in the lattice fringe spacings. The corresponding SAED pattern is added and indexed using the ZnO cell parameters.

of the simulated pattern background. Note that the background becomes more and more asymmetric (consequently, the quality of the fit decreases) when the zinc content increases. The ZN15 sample simulation evidences such a strong misfit between the experimental and calculated background, while the FWHM of the main peak seems to be correctly calculated. Nevertheless, the harmonics forming the asymmetric background on the simulated pattern are often the exaggerated representation of some phenomena on the experimental pattern. Note the large left shoulder on the ZN7 sample pattern (ZN7, circled region, Fig. 12), which corresponds to harmonics fading when 2θ decreases. Again, this is most likely due to preferential orientation of the film.

Finally, it is worth noting that, for a few samples, the FWHM on the main Bragg peak is underestimated on the simulated pattern (Fig. 12, ZN3). The origin of the misfit could be due to the nonrepresentativeness of the crystals studied by HRTEM. Data used for the ZN3 sample come

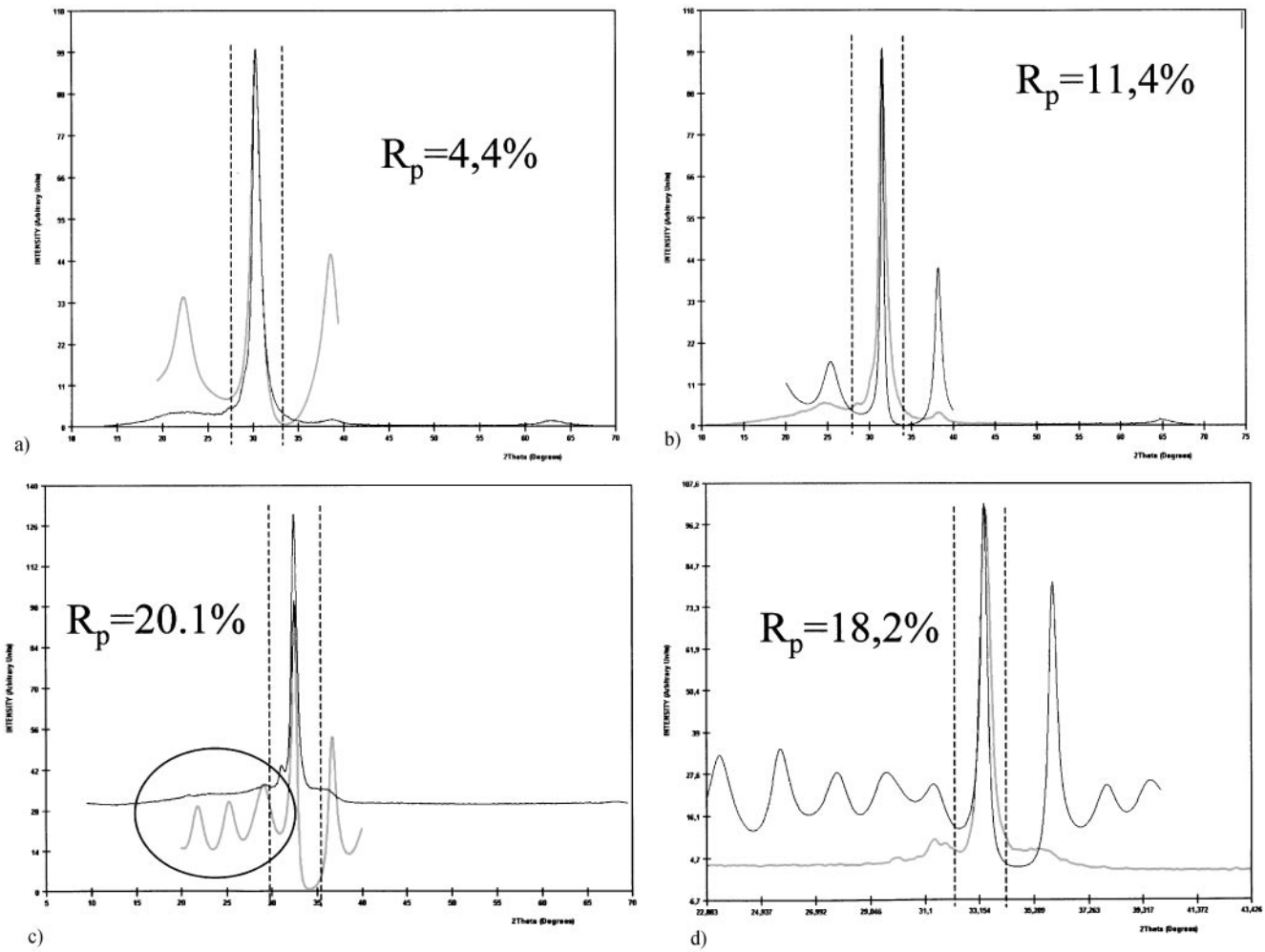

FIG. 12. Simulated X-ray diffraction patterns superimposed on the experimental patterns obtained on (a) ZN2 ($x = 0.5$), (b) ZN3 ($x = 0.6$), (c) ZN7 ($x = 0.78$), and (d) ZN15 ($x = 0.88$) films samples. The R_p value, noted in the graph, is calculated between the 2θ values delimited by vertical lines.

from many crystals containing completely different proportions of polytypes. This confirms that a few thin-film samples, obtained by PLD, are poorly homogeneous.

CONCLUSION

The HRTEM technique has enabled the full structural/textural characterization of PLD films, the compositions of which pertain to the In_2O_3–ZnO binary system. Additionally, we succeeded, by electron microscopy techniques, in isolating three distinct structural/textural types films. Two techniques give the structure and texture of the end-member phases while the third one presents a fiber texture made of a multitude of $Zn_kIn_2O_{k+3}$ polytypes. The latter are highly polyphasic and mostly composed of the polytype having the target composition. Furthermore, this study showed that the mono- or polyphasic character of the target has no impact on the $Zn_kIn_2O_{k+3}$ films obtained by PLD. To our knowledge, this is the first time this last technique has enabled the stabilization of $Zn_2In_2O_5$ and other polytypes that could not be synthesized in the bulk state. Finally, using HRTEM structural information, we succeeded in simulating and explaining the thin-film XRD spectra that were reported in the literature but for which explanations were not given. The importance of this structural information about the physical properties of these films, namely resistivity and optical transparence, will be reported in a forthcoming paper.

ACKNOWLEDGMENTS

The authors thank Alexandra Blyr, Corinne Marcel, and Aline Rougier for their useful discussions, and are indebted to the CRISMAT of Caen for enabling the HRTEM studies, with special thanks to M. Hervieu and B. Mercey for their technical discussions and expertise.

REFERENCES

1. G. B. Palmer, K. R. Poeppelmeier, and T. O. Mason, *Chem. Mater.* **9,** 3121 (1997).
2. Z. C. Jin, I. Hamber, and C. G. Granqvist, *J. Appl. Phys.* **64,** 5117 (1988).
3. D. D. Edwards, T. O. Mason, F. Goutenoire, and K. R. Poeppelmeier, *Appl. Phys. Lett.* **70,** 1706 (1997).
4. R. Wang, L. L. H. King, and A. W. Sleight, *J. Mater. Res.* **11,** 1659 (1996).
5. X. Wu, T. J. Coutts, and W. P. Milligan, *J. Vac. Sci. Technol. A* 1057 (1997).
6. Z. Y. Nong, S. H. Cheng, S. B. Ge, Y. Chao, Z. Q. Gang, Y. X. Zhang, and Z. G. Liu, *Thin Solid Films* **307,** 50 (1997).
7. T. Minami, T. Kakumu, and H. Sonohara, *Thin Solid Films* **22,** 270 (1995).
8. C. Schinzer, F. Heyd, and S. F. Matar, *J. Mater. Chem.* **9,** 1569 (1999).
9. N. Naghavi, C. Marcel, L. Dupont, A. Rougier, J.-B. Leriche, and C. Guery, *J. Mater. Chem.* **10,** 2315 (2000).
10. N. Naghavi, A. Rougier, C. Marcel, J. B. Leriche, and J. M. Tarascon, *Thin Solid Films* **360,** 233 (2000).
11. T. Moriga, D. Edwards, T. O. Mason, G. B. Palmer, K. R. Poeppelmeier, J. Schindler, C. Kannewurf, and I. Nakabayashi, *J. Am. Ceram. Soc.* **81,** 1310 (1998).
12. A. Wang, J. Dai, J. Cheng, M. P. Chuzik, T. J. Marks, R. P. H. Chang, and C. R. Kannewurf, *Appl. Phys. Lett.* **73**(3), 327 (1998).
13. C. Li, Y. Bando, M. Nakamura, and N. Kimizuka, *J. Electron Microsc.* **46**(2), 119 (1997).
14. V. H. Kasper, *Z. Anorg. Allg. Chem.* **349,** 113 (1967).
15. C. Li, Y. Bando, M. Nakamura, M. Onoda, and N. Kimizuka, *J. Solid State Chem.* **139,** 347 (1998).
16. N. Kimizuka, M. Isobe, and M. Nakamura, *J. Solid State Chem.* **116,** 170 (1995).
17. C. Li, Y. Bando, M. Nakamura, and N. Kimizuka, *Z. Kristallogr.* **214,** 528 (1999).
18. S. Hendricks and E. Teller, *J. Chem. Phys.* **10,** 147 (1942).
19. R. W. G. Wyckoff, "Crystal Structures," 2nd Ed. Vol. 2, p. 2, Wiley, New York, 1964.
20. S. Abrahams and J. Bernstein, *Acta Crystallogr. B* **25,** 1233 (1969).
21. J. L. Hutchison and A. J. Jacobson, *Acta Crystallogr. B* **31,** 1442 (1975).
22. J. L. Hutchison and A. J. Jacobson, *J. Solid State Chem.* **20,** 417 (1977).
23. J. L. Hutchison and A. J. Jacobson, *J. Solid State Chem.* **35,** 334 (1980).
24. P. J. Cannard and R. J. D. Tilley, *J. Solid State Chem.* **73,** 418 (1988).
25. P. Scherrer, *Nachr. Ges. Wiss. Göttingen* 98 (1918).
26. I. Sieber, N. Wanderka, I. Urban, I. Dörfel, E. Schrierhorn, F. Fenske, and W. Fuhs, *Thin Solid Films* **330,** 108 (1998).